Phase-field crystal model for a diamond-cubic structure

V. W. L. Chan, N. Pisutha-Arnond, and K. Thornton

Phys. Rev. E **91**, 053305 — Published 14 May 2015

DOI: 10.1103/PhysRevE.91.053305

Phase-Field Crystal Model for Diamond-Cubic Structure

V. W. L. Chan,[1,*] N. Pisutha-Arnond,[2,†] and K. Thornton[1,‡]

[1] *Materials Science and Engineering Department, University of Michigan, Ann Arbor, Michigan, 48109, USA*

[2] *Department of Industrial Engineering, Faculty of Engineering, King Mongkut's Institute of Technology Ladkrabang, Bangkok, Thailand*

(Dated: April 17, 2015)

Abstract

We present a structural phase-field crystal (XPFC) model [Greenwood et al. PRL 105, 045702 (2010)] that yields a stable *dc* structure. The stabilization of a *dc* structure is accomplished by constructing a two-body direct correlation function (DCF) approximated by a combination of two Gaussian functions in Fourier space. A phase diagram containing a *dc*-liquid phase coexistence region is calculated for this model. We examine the energies of solid-liquid interfaces with normals along the [100], [110], and [111] directions. The dependence of interfacial energy on a temperature parameter, which controls the heights of the peaks in the two-body DCF, is described by a Gaussian function. Furthermore, the dependence of interfacial energy on peak widths of the two-body DCF, which controls the excess energy associated with interfaces, defects, and strain, is described by an inverse power law. These relationships can be used to parameterize the PFC model for the *dc* structure to match solid-liquid interfacial energies to those measured experimentally or calculated from atomistic simulations.

* vicchan@umich.edu

† kpnirand@kmitl.ac.th

‡ kthorn@umich.edu

I. INTRODUCTION

The phase-field crystal (PFC) model was developed to study atomististic-scale phenomena that occur at experimentally observable time scales. Since its first demonstration in 2002, the model has been applied to study important materials phenomena such as dislocation dynamics [1–3], nucleation [4, 5], and grain boundary energy anisotropy [6, 7], albeit on a qualitative level. A step toward a more quantitative PFC model was undertaken by Elder et al. in 2007 when they derived the free energy of the PFC model from that of the classical density functional theory (cDFT) of freezing via several approximations [8]. The link between PFC and cDFT provided a microscopic interpretation of the PFC model parameters and established a connection between the PFC model and experimentally measured structure factors through the two-body direct correlation function (DCF).

The two-body DCF dictates the spatial configuration of the order parameter in the PFC model, which is important for describing elastic and plastic deformations, as well as anistropy of solid-solid and solid-liquid interfaces. Therefore, much research in the PFC literature has been focused on modifying the two-body DCF to improve the predictive capability of the model. As a result, several new formulations for representing the two-body DCF have been developed. For example, Jaatinen et al. fit the two-body DCF in Fourier space up to the first peak using an eighth-order polynomial function to quantitatively study body-centered-cubic (*bcc*) Fe [9]. Pisutha-Arnond et al. fit the two-body DCF beyond the first peak with a rational function to examine the predictive capability of the cDFT of freezing [10]. Furthermore, Greenwood et al. constructed two-body DCFs in Fourier space using Gaussian peaks to systematically stabilize various crystal structures [11, 12].

In this work we focus on the structural PFC (XPFC) model developed by Greenwood et al. [11, 12] because of the model's capability to produce a range of crystal structures in a systematic and straightforward manner. This model has been shown to stabilize crystal structures such as *bcc*, face-centered cubic (fcc), simple cubic (sc), and hexagonal close-packed (hcp) structures [12] and has been used to study many phenomena including solute drag effects on grain boundary motion [13], clustering and precipitation in an Al-Cu alloy [14, 15], and the stability of stacking faults and partial dislocations [16]. However, a diamond-cubic (dc) structure, to the knowledge of the authors, had not been shown to be stable within the PFC model. As a result, semiconductor materials, such as Si and Ge, have not been

studied in three dimensions.

Therefore, we have developed a PFC model with a stable *dc* structure, which is based on the XPFC approach. To this end, we approximate a two-body DCF with a combination of two Gaussian functions in Fourier space, with the first and second peak positions centered at $k_1 = 2\pi\sqrt{3}/a$ and $k_2 = 2\pi\sqrt{8}/a$, respectively, where a is the lattice constant of a cubic structure, and k_1 and k_2 are magnitudes of wave vectors. A temperature-density phase diagram that contains a *dc* solid-liquid coexistence region is then calculated for this model. It is worth noting that a recent model for self assembly [17], which resembles the PFC model, was shown to also stabilize a *dc* structure with a long-range interaction term that enforces the coordinates of a desired structure in Fourier space. Although, the ability to explicitly enforce the coordinates of a structure provides the capability of stabilizing very complex structures (e.g., a double-helix structure [17]), the orientation of the crystal is fixed by the orientation of the coordinates. Therefore, rotational invariance, which is retained in the PFC model and is important for studying polycrystalline systems, is lost.

For the model to be applied to a specific material, it is critical that it reproduces material properties such as interfacial energies and elastic behavior, as well as the bulk energetics reflected in the phase diagram. In the latter part of this paper, we focus on the interfacial energies, including the interfacial anisotropy that arises naturally in the PFC model. We examine how the solid-liquid interfacial energy of the *dc* structure depends on the shape of the DCF within the *dc*-PFC model. A relationship for solid-liquid interfacial energy as a function of temperature is developed for the *dc* structure by taking the peak heights of the Gaussian functions in the two-body DCF to change with a temperature parameter according to the functional form of the Debye-Waller Factor [11]. Additionally, since the energy change due to interfaces, defects, and strain is controlled by the peak width of the Gaussian functions [11], relationships for the dependence of interfacial energies on peak widths are also determined. These relationships can be used to parameterize the *dc*-PFC model to match interfacial energies to those measured experimentally or calculated from atomistic simulations.

The paper is outlined as follows. We begin by providing background of the XPFC model in section II, where the parameters of the DCF are discussed in detail. A procedure for constructing phase diagrams in the PFC model is described in section III, and is used to calculate a phase diagram for the *dc* structure. The phase diagram contains *dc*-liquid

coexistence region, enabling us to numerically examine the solid-liquid interfacial properties of the *dc* structure in section IV. Relationships between the interfacial energy and the peak widths and heights of the Gaussian functions in the DCF are also developed in section IV. Finally, we summarize the results of our work and present potential direction for future work in section V.

II. THE STRUCTURAL PHASE-FIELD CRYSTAL (XPFC) MODEL

The PFC free energy is based on a free-energy difference with respect to a liquid reference state and can be derived from the cDFT of freezing [8]. The free energy is written in terms of an ideal-gas contribution, $\Delta\mathcal{F}_{id}[n(\mathbf{r})]$, which is derived from a non-interacting system of particles, and an excess contribution, $\Delta\mathcal{F}_{ex}[n(\mathbf{r})]$, which contains the description of the interactions between particles

$$\Delta\mathcal{F}[n(\mathbf{r})] = \Delta\mathcal{F}_{id}[n(\mathbf{r})] + \Delta\mathcal{F}_{ex}[n(\mathbf{r})]. \tag{1}$$

The Δ symbol in Eq. (1) indicates a free-energy difference from a state that is at a reference liquid density, ρ_0. The variable $n(\mathbf{r})$ is the scaled dimensionless number density and is related to the atomic-probability density, $\rho(\mathbf{r})$, by $n(\mathbf{r}) \equiv \rho(\mathbf{r})/\rho_0 - 1$.

The ideal-gas contribution,

$$\Delta\mathcal{F}_{id}[n(\mathbf{r})] = \rho_0 k_B T \int \left[\frac{n(\mathbf{r})^2}{2} - \frac{n(\mathbf{r})^3}{6} + \frac{n(\mathbf{r})^4}{12}\right] d\mathbf{r}, \tag{2}$$

where k_B and T are the Boltzmann constant and temperature, respectively, is minimized by $n(\mathbf{r})$ that is equal to a constant value. Regions where $n(\mathbf{r})$ is constant are considered to be in the liquid state. On the other hand, depending on the choice of a two-body DCF, $C^{(2)}$, the excess contribution,

$$\Delta\mathcal{F}_{ex}[n(\mathbf{r})] = -\frac{\rho_0^2 k_B T}{2} \int n(\mathbf{r}) \left[\int C^{(2)}(\mid \mathbf{r} - \mathbf{r}' \mid) n(\mathbf{r}') d\mathbf{r}'\right] d\mathbf{r}, \tag{3}$$

is minimized by $n(\mathbf{r})$ that contains peaks with the periodicity of a crystal lattice. Regions where $n(\mathbf{r})$ takes this form are considered to be a crystalline solid. In expressing the two-body DCF as $C^{(2)}(\mid \mathbf{r} - \mathbf{r}' \mid)$, an assumption has been made that the two-body DCF is isotropic [8].

The two-body DCF, which is the key quantity that gives rise to stability of crystalline phases in Eq. (3), is typically expressed in Fourier space [8–11]. As a result, the convolution

theorem can be used to evaluate the inner integral (with respect to $\mathbf{r}'$) of Eq. (3) in the form of the inverse Fourier transform of the product of Fourier transforms,

$$\Delta\mathcal{F}_{ex}[n(\mathbf{r})] = -\frac{\rho_0^2 k_B T}{2} \int n(\mathbf{r}) \mathscr{F}^{-1}\left[\hat{C}^{(2)}(k)\,\hat{n}(\mathbf{k})\right] d\mathbf{r}, \tag{4}$$

where $k = |\mathbf{k}|$, the notation $\mathscr{F}^{-1}[\ ]$ is the inverse Fourier-transform operation, and the hat symbols denote Fourier transforms of the quantities.

In the XPFC model, the two-body DCF is approximated by a combination of modulated Gaussian functions in Fourier space via [11, 12]

$$\hat{c}^{(2)}(k) = \rho_0 \hat{C}^{(2)}(k) = \max\left(G^i(k), G^{i+1}(k), \ldots, G^N(k)\right), \tag{5}$$

where N is the total number of Gaussian functions used in the approximation of the DCF, and

$$G^i(k) = \exp\left(-\frac{\sigma^2 k_i^2}{2\lambda_i \beta_i}\right) \exp\left(-\frac{(k-k_i)^2}{2\alpha_i^2}\right) \tag{6}$$

is the modulated Gaussian function (i.e., a Gaussian function with its height modified by an exponential function). The subscripts and superscripts i denote the i^{th} family of crystallographic planes that are being considered; the families of planes are typically enumerated in order of decreasing interplanar spacings, where $i = 1$ corresponds to the family of crystallographic planes with the largest interplanar spacing. The parameter k_i specifies the position of the i^{th} Gaussian peak and the value of k_1 corresponds to the reciprocal lattice spacing of a crystal structure; α_i corresponds to the root-mean-square width of the i^{th} Gaussian peak and controls the excess energy associated with defects, interfaces, and strain [11]; σ controls the heights of the Gaussian peaks and is related to temperature [11]; λ_i and β_i are the planar atomic density and the number of planar symmetries of the i^{th} family of crystallographic planes, respectively, and control how much the height of the Gaussian functions change when σ is adjusted. Since the parameter k_i also exists in the exponential term in front of the Gaussian functions in Eq. (6), k_i also affects the change in the height of the Gaussian functions when σ is adjusted. Note that σ is a parameter related to temperature, but should not be interpreted to be equal to temperature.

Each value of k_i sets the interplanar spacing, L_i, for a family of crystallographic planes within a crystal structure; specifically, $k_i = 2\pi/L_i$. For example, the k_1 and k_2 values for a *bcc* structure corresponds to the {110} and {200} families of planes, respectively, and have values of $k_1 = 2\pi\sqrt{2}/a_{bcc}$ and $k_2 = 4\pi/a_{bcc}$, where a_{bcc} is the lattice constant of the *bcc*

structure. On the other hand, the k_1 and k_2 values for an fcc structure correspond to the $\{111\}$ and $\{200\}$ families of planes, respectively, and have values of $k_1 = 2\pi\sqrt{3}/a_{fcc}$ and $k_2 = 4\pi/a_{fcc}$, where a_{fcc} is the lattice constant of the fcc structure.

As demonstrated by Greenwood et al. [12], the XPFC model for the *bcc* structure can be constructed with a two-body DCF that is approximated with a single Gaussian function centered at $k_1 = 2\pi\sqrt{2}/a_{bcc}$ in Fourier space. On the other hand, the fcc structure is stabilized by two Gaussian functions centered at $k_1 = 2\pi\sqrt{3}/a_{fcc}$ and $k_2 = 4\pi/a_{fcc}$ at sufficiently low temperatures. Note that the ratio of the peak positions of the fcc structure, $k_2/k_1 = \sqrt{4/3}$, is independent of a_{fcc}.

III. PHASE STABILITY OF A DIAMOND-CUBIC STRUCTURE

In this section, we demonstrate that the XPFC model can be used to stabilize the *dc* crystal structure. We also examine the phase stability between *dc* and other phases to construct a temperature-density phase diagram. First, we describe the procedure for constructing a phase diagram with the PFC model [11, 12, 18], which is used in this work. We then introduce a two-body DCF that stabilizes a *dc* structure and construct a temperature-density phase diagram that consists of the *bcc*, *dc*, and liquid phases based on the model.

A. Procedure for Constructing a Phase Diagram

A phase diagram for the PFC model is constructed by finding the average of the scaled dimensionless number density, $\bar{n}$, that corresponds to the phase boundaries as a function of σ [11, 12, 18]. The procedure for identifying the phase boundaries for each value of σ is divided into two steps. First, free-energy densities as a function of $\bar{n}$ are calculated for each phase by minimizing the free-energy density, $\Delta f^{\alpha}(\bar{n}, a)$, with respect to a, where the superscript α denotes the phase (e.g., $\alpha = bcc$, fcc, dc). The quantity $\Delta f^{\alpha}(\bar{n}, a)$ is calculated via,

$$\Delta f^{\alpha}(\bar{n}, a) \equiv \frac{\Delta \mathcal{F}^{\alpha}[n_a(\mathbf{r})]}{V_a}, \tag{7}$$

where $V_a \equiv a^3$ is the unit-cell volume, a is the lattice parameter of a cubic unit cell, and $n_a(\mathbf{r})$ is the relaxed density profile. The relaxed density profile is obtained by evolving a (non-relaxed) density profile that is approximated with the one-mode approximation with

an average of $\bar{n}$ using conserved dissipative dynamics [6, 8, 19],

$$\frac{\partial n(\mathbf{r})}{\partial t} = \nabla^2 \frac{\delta \Delta \mathcal{F}^{\alpha}[n(\mathbf{r})]}{\delta n(\mathbf{r})}, \tag{8}$$

until a steady state is reached. The quantity $\Delta f^{\alpha}(\bar{n}, a)$ is a function of only $\bar{n}$ and a because $\Delta f^{\alpha}(\bar{n}, a)$ is the free-energy density of a system with $n_a(\mathbf{r})$, which is periodic with a uniform amplitude. For convenience, we denote the value of $\Delta f^{\alpha}(\bar{n}, a)$ that is minimized with respect to a as $\Delta f^{\alpha}_{a^*}(\bar{n})$ and the corresponding lattice spacing as a^*. This process is schematically illustrated in Fig. 1(a) where the point $(a^*, \Delta f^{\alpha}_{a^*}(\bar{n}))$ is marked with "×".

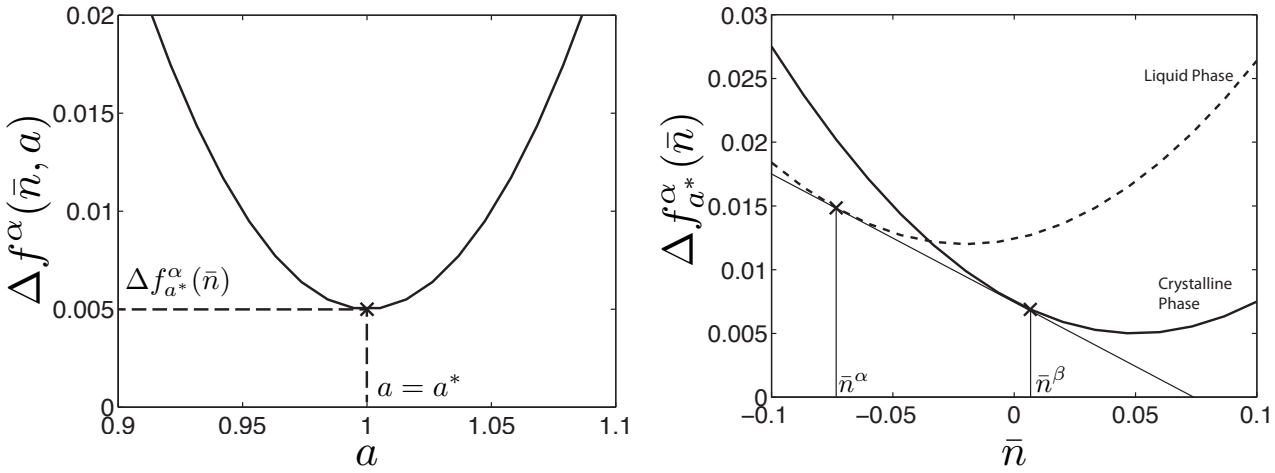

(a) (b)

FIG. 1. (a) Schematic plot of free-energy density of a relaxed system as a function of the lattice spacing for a given $\bar{n}$. The point at which $\Delta f^{\alpha}(\bar{n}, a)$ is minimized with respect to a is marked with "×". (b) Schematic of the free-energy densities that satisfy $\partial \Delta f^{\alpha}(\bar{n}, a)/\partial a = 0$ at each $\bar{n}$ (as illustrated in (a)). The solid curve shows the free-energy density for the crystalline phase, and the dashed curve shows the corresponding values for the liquid phase. The "×" denotes the comment-tangent points of the free-energy density curves, which satisfy Eqs. (9) and (10).

Second, phase boundaries are determined with a common-tangent construction on the convex hull [20] of $\Delta f^{\alpha}_{a^*}(\bar{n})$ for all phases. The common-tangent construction is mathematically stated as a set of conditions:

$$\left.\frac{\partial \Delta f^{\alpha}_{a^*}(\bar{n})}{\partial \bar{n}}\right|_{\bar{n}=\bar{n}^{\alpha}} = \left.\frac{\partial \Delta f^{\beta}_{a^*}(\bar{n})}{\partial \bar{n}}\right|_{\bar{n}=\bar{n}^{\beta}} \tag{9}$$

and

$$\Delta f^{\beta}_{a^*}(\bar{n}) - \Delta f^{\alpha}_{a^*}(\bar{n}) = \left.\frac{\partial \Delta f^{\alpha}_{a^*}(\bar{n})}{\partial \bar{n}}\right|_{\bar{n}=\bar{n}^{\alpha}} (\bar{n}^{\beta} - \bar{n}^{\alpha}). \tag{10}$$

The additional superscript, β, denotes a phase different from that indicated by α (e.g., $\alpha = bcc$ and $\beta = fcc$) and the partial derivatives are evaluated at the specified value of $\bar{n}$, as indicated by the subscripts on the vertical line. Equations (9) and (10) ensure that the chemical potentials and pressures of the coexisting phases, respectively, are equal [18]. The conditions of Eqs. (9) and (10) are illustrated in Fig. 1(b), where "×" marks the common-tangent points. The procedure described above is repeated for different values of σ to construct a phase diagram.

B. A Diamond-Cubic Structure

A *dc* structure is an *fcc* derivative structure that consists of the lattice-sites of two *fcc* structures that are shifted from one another by $a_{fcc}/4$ in each direction [21]. The lattice-site positions of the two *fcc* structures are specified by two basis vectors. The two *fcc* structures within a single *dc* unit cell are illustrated in Fig. 2(a).

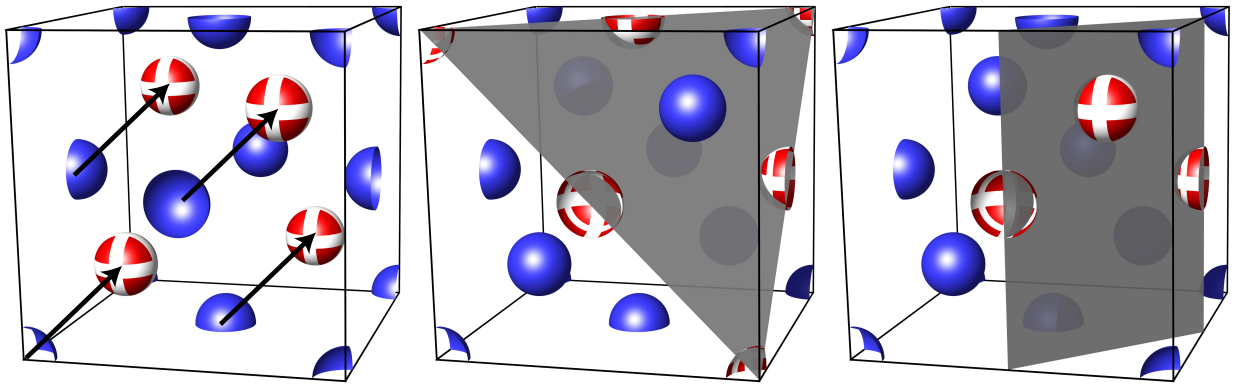

(*a*) (*b*) (*c*)

FIG. 2. (Color online) (a) Schematic of a unit cell of the *dc* structure where the shift of $a_{fcc}/4$ in each direction between the lattice-site positions of two *fcc* structures (one colored in solid blue and the other colored in red overlaid with white stripes) is denoted by arrows. Schematics of the (b) (111) and (c) (220) crystallographic planes, where the lattice points that are intersected by the atomic planes are highlighted in red and overlaid with white stripes. Each plane of the {111} and {220} families of planes intersect 2 atoms for the *dc* structure.

We find that a two-body DCF approximated with the combination of two Gaussian functions centered at $k_1 = 2\pi\sqrt{3}/a_{dc}$ and $k_2 = 2\pi\sqrt{8}/a_{dc}$ will stabilize a *dc* structure.

The values of $k_1 = 2\pi\sqrt{3}/a_{dc}$ and $k_2 = 2\pi\sqrt{8}/a_{dc}$ correspond to the $\{111\}$ and $\{220\}$ families of crystallographic planes, which are associated with the first two peaks of the *dc* structure factor [21]. As in the fcc structure, the ratio of peak positions of the *dc* structure, $k_2/k_1 = \sqrt{8/3}$, is independent of a_{dc}. An fcc structure is not stable for this DCF because it does not contain a peak corresponding to the $\{200\}$ family of crystallographic planes, which is required for the stabilization of an fcc structure [12].

To construct a phase diagram for the *dc* structure, we choose $a_{dc} = 1\mathring{A}$ and $\alpha_1 = \alpha_2 = 1.0$. The $\{111\}$ and $\{220\}$ families of crystallographic planes of the *dc* structure contain 8 and 12 equivalent planes, respectively. Therefore, the parameters β_1 and β_2, which are the number of planar symmetries of the $\{111\}$ and $\{220\}$ families of crystallographic planes, are 8 and 12, respectively. Each plane of the $\{111\}$ and $\{220\}$ families of planes have an area of $\sqrt{3}/2 \times a_{dc}^2$ and $\sqrt{2}/2 \times a_{dc}^2$, respectively, and intersects 2 atoms in the *dc* structure, as shown in Figs. 2(b) and (c). Therefore, the parameters λ_1 and λ_2 are $2/(\sqrt{3}/2) = 4/\sqrt{3}\mathring{A}^{-2}$ and $2/(\sqrt{2}/2) = 2\sqrt{2}\mathring{A}^{-2}$, respectively.

The *dc* DCF in Fourier space is plotted for $\sigma = 0.0$, 0.2, and 0.4 in Fig. 3(a) for the values of k_i, λ_i, β_i, and α_i mentioned above. The stability of the *dc* structure was verified by comparing the unit-cell free-energy density of the *dc* structure to those of the *bcc*, fcc, *sc*, *hcp*, rod, and stripe phases [18]. Additionally, the stability of the *dc* structure for calculations beyond a unit cell was demonstrated by the growth of an 18 $(2 \times 3 \times 3)$ unit-cell *dc* seed into a 64 unit-cell system for $\sigma = 0.01$ and $\bar{n} = 0.02$ via Eq. (8); the initial seed was generated by appending relaxed unit cells of the *dc* structure. The isosurface of the relaxed 64 unit cell system is shown in Fig. 3(b) and a small portion of the system is extracted in Fig. 3(c) to illustrate two overlapping fcc lattices in the *dc* structure. It is important to note that a metastable *bcc* structure forms when the initial seed size is smaller than 18 unit cells for the 64 unit-cell system considered in Fig. 3(b). This suggests that the density profile can converge to a metastable structure (*bcc*) instead of the stable structure (*dc*) when the dynamics described by Eq. (8) is used to evolve the density field. The formation of a metastable *bcc* phase prior to forming a stable *dc* phase was also observed in a recently proposed self-assembly model [17]. An investigation of different dynamics for the PFC model is outside the scope of this paper. We refer the readers to Ref. [22] for an overview of various PFC dynamics.

A density-temperature phase diagram, shown in Fig. 3(d), is constructed according to

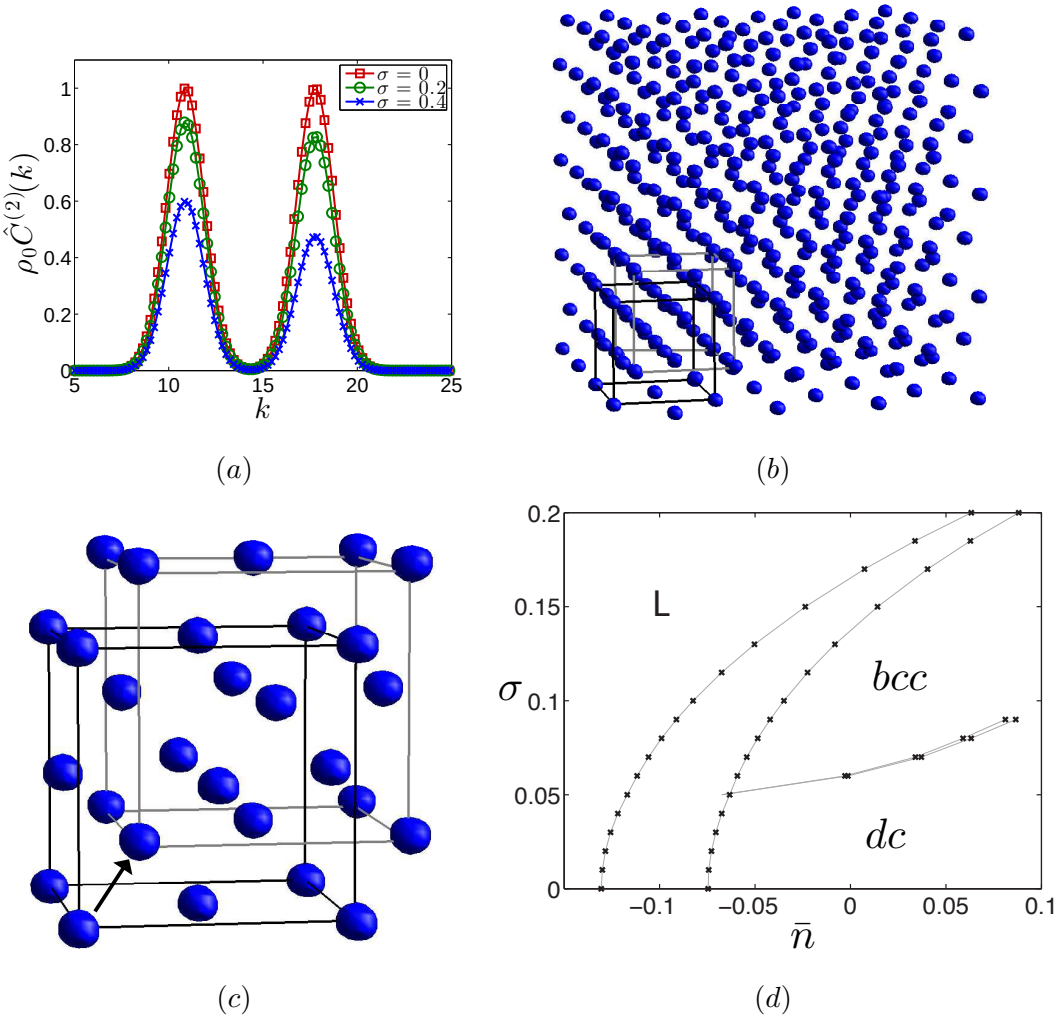

FIG. 3. (Color online) (a) The two-body DCF for a *dc* structure for $\sigma = 0.0$, 0.2, and 0.4. The parameters used are $\alpha_1 = \alpha_2 = 1.0$, $\lambda_1 = 4/\sqrt{3}\mathring{A}^{-2}$, $\lambda_2 = 4/\sqrt{2}\mathring{A}^{-2}$, $\beta_1 = 8$, $\beta_2 = 12$, $k_1 = 2\pi\sqrt{3}\mathring{A}^{-1}$, and $k_2 = 2\pi\sqrt{8}\mathring{A}^{-1}$. (b) The isosurface of a 64 unit-cell *dc* structure calculated for $\bar{n} = 0.02$ and $\sigma = 0.01$. (c) Small portion of Fig. (b) showing two overlapping fcc lattices in a *dc* structure. The black arrow denotes the shift of a lattice site from one fcc lattice to the other. (d) Phase diagram containing body-centered-cubic (*bcc*), diamond-cubic (*dc*), and liquid (L) phases.

the procedure presented in section III A. The phase diagram shows a stable liquid phase at low densities and solid phases at higher densities. The coexistence between liquid and *dc*, liquid and *bcc*, and *bcc* and *dc* phases are also shown in Fig. 3(d). Since k_1 corresponds to the {111} family of planes in the *dc* structure and the {110} family of planes in the *bcc* structure, the lattice constant of the *dc* and *bcc* structures are different and related to one

another by $a_{bcc}/a_{dc} = \sqrt{2/3}$.

The small gap between the *bcc* and *dc* coexisting densities is due to the similarity between the free-energy densities of the two solid phases. The similarity in the coexisting densities is undesirable, for example, when studying solid defects in a two-phase system. To alter the energy of each phase and thus potentially increase the gap of the solid-coexistence densities, one can modify, in addition to the two-body DCF, the ideal-gas contribution to the free energy in Eq. (2) [9]. This will be investigated in the future.

An important feature of the phase diagram in Fig. 3(d) is the *dc*-liquid coexistence at lower temperatures and the *bcc*-liquid coexistence at higher temperatures. A *bcc* phase becomes stable for a two-peak DCF when the the first peak is significantly taller than the second peak, as described in Ref. [12]. When the parameters in Eq. (6) are chosen to be

$$\frac{\lambda_1\beta_1}{\lambda_2\beta_2} > \left(\frac{k_1}{k_2}\right)^2, \tag{11}$$

the first peak of the DCF becomes taller than the second peak as σ increases (e.g., see Fig. 3(a)). The parameters used to construct the phase diagram of Fig. 3(d) has $(\lambda_1\beta_1)/(\lambda_2\beta_2) = 1.45(k_1/k_2)^2$, and thus a transition from the *dc* phase at lower temperatures to the *bcc* phase at higher temperatures is observed.

On the other hand, the *bcc* phase can be suppressed at all temperatures if the height of the first and second peaks of a two-peak DCF are constrained to be equal for all values of σ. This occurs when

$$\frac{\lambda_1\beta_1}{\lambda_2\beta_2} = \left(\frac{k_1}{k_2}\right)^2. \tag{12}$$

A phase diagram where Eq. (12) is satisfied is plotted in Fig. 4; as expected, the *bcc* phase has been suppressed.

IV. SOLID-LIQUID INTERFACIAL ENERGY

We examine the solid-liquid interfacial energies of the *dc* structure described in the previous section. First, we describe a numerical procedure for calculating interfacial energy between two phases. Second, we determine a relationship for interfacial energy as a function of Gaussian peak width because the peak widths of the Gaussian functions in the DCF were shown to account for excess energy due to interfaces [11]. Third, we develop a relationship for interfacial energy as a function of temperature by adjusting peak height. Finally, we

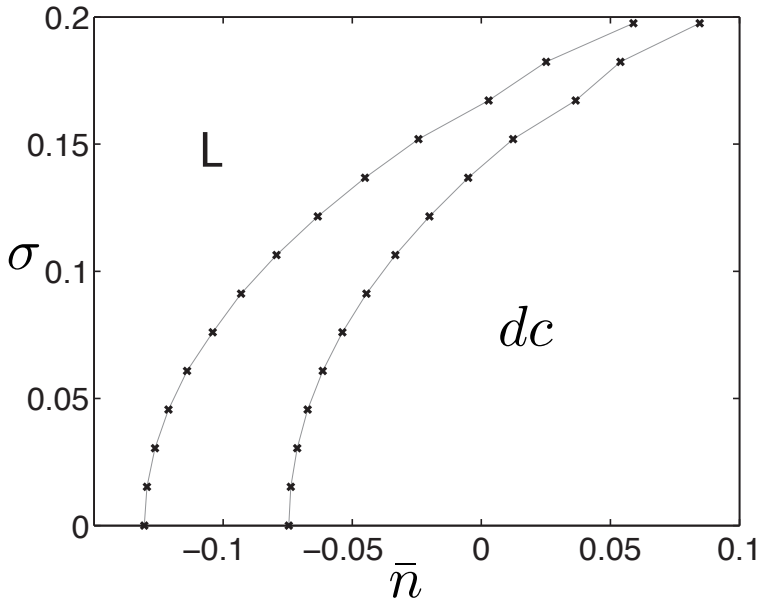

FIG. 4. Phase diagram containing diamond-cubic (*dc*) and liquid (L) phases. The parameters of the two-body DCF used to construct this phase diagram are $\alpha_1 = \alpha_2 = 1.0$, $\lambda_1 = 4/\sqrt{3}\mathring{A}^{-2}$, $\beta_1 = 8$, $k_1 = 2\pi\sqrt{3}\mathring{A}^{-1}$, $k_2 = 2\pi\sqrt{8}\mathring{A}^{-1}$, and $\lambda_2\beta_2 = 8/3\lambda_1\beta_1$.

consider a more general case of two-body DCFs where the first and second peaks of the Gaussian functions have different widths. This analysis provides an approximate relationship between interfacial energy and peak width of the Gaussian functions when the peak widths are not equal. For the analysis below, k_i, λ_i, and β_i are set to the values that were used to construct the phase diagram in Fig. 3(d).

A. Procedure for Numerical Calculation of Solid-Liquid Interfacial Energy

The interfacial energy of a system that is in solid-liquid coexistence state can be calculated from the energy of the two-phase system minus the bulk energy of each phase [9]. In this section, the solid-liquid interfacial energy of an interface having a normal pointing in the direction p, γ_p, is evaluated by constructing a long slab of one unit-cell in the plane of the interface and 128 unit-cells in the direction of the interface normal. The slab is initialized with 64 unit cells of solid and 64 unit cells of liquid, with the interface at the midpoint of the computational domain. Periodic boundary conditions are applied to all boundaries, which places another interface at the ends of the length of the computational domain. The slab is

then numerically relaxed via Eq. (8). The value of γ_p is determined from the numerically relaxed slab by subtracting the free energy of the bulk phases from the total free energy of the slab and dividing by the cross-sectional area of the solid-liquid interface.

The bulk free energy, $\Delta\mathcal{F}^{bulk}$, is calculated from the free energies of solid with the same volume as the computational domain, $\Delta\mathcal{F}_s$, and liquid with the same volume as the computational domain, $\Delta\mathcal{F}_l$. These free energies are weighted by the volume fraction before they are summed. Therefore, with the average of the scaled number densities of the solid and liquid at the coexistence density, $\bar{n}_s$ and $\bar{n}_l$, respectively, $\Delta\mathcal{F}^{bulk}$ is given by

$$\Delta\mathcal{F}^{bulk} = \frac{\Delta\mathcal{F}_s(\bar{n} - \bar{n}_l) + \Delta\mathcal{F}_l(\bar{n}_s - \bar{n})}{\bar{n}_s - \bar{n}_l}, \tag{13}$$

where the weighing of $\Delta\mathcal{F}_s$ and $\Delta\mathcal{F}_l$ is determined according to volume fractions of solid and liquid in the system in terms of the respective densities. The value of γ_p is then calculated by subtracting $\Delta\mathcal{F}^{bulk}$ from the total free energy of the slab containing the solid-liquid interfaces, $\Delta\mathcal{F}_p^{slab}$, and dividing by the cross-sectional area, A_p,

$$\gamma_p = \frac{1}{\rho_0 k_B T}\left(\frac{\Delta\mathcal{F}_p^{slab} - \Delta\mathcal{F}^{bulk}}{2A_p}\right), \tag{14}$$

where the factor, $1/(\rho_0 k_B T)$, nondimensionalizes the value of γ_p and the factor of 2 accounts for the additional interface at the edge of the computational domain due to the periodic boundary conditions. The length of the slab in the direction of the interface normal is chosen such that the two solid-liquid interfaces that form as a result of periodic boundary conditions do not interact. In this work, we examine the γ_p of interfaces with normals pointing in the [100], [110], and [111] directions, where $p = 100, 110$, and 111, respectively. This analysis is performed on an XSEDE computing cluster [23].

B. Solid-Liquid Interfacial Energy Dependence on the Peak-Width

We use the procedure described in section IV A to compare the solid-liquid interfacial energies, $\gamma_p(\sigma, \alpha_1, \alpha_2)$, for different peak widths, α_i, of the Gaussian functions in the two-body DCF. The calculations presented here are for the *dc* DCF used to construct Fig. 3(d) with $\sigma = 0$, which leads to both peak heights to be 1, and $\alpha_1 = \alpha_2 \equiv \alpha_0$, which sets the peak widths equal. The value of $\gamma_p(0, \alpha_0, \alpha_0)$ for the (100), (110), and (111) interfaces for values of α_0 ranging from 0.25 to 1.0 are plotted in Fig. 5. These interfacial energies decrease

with increasing values of α_0. For the range of α_0, the (111) interface has the lowest energy, while the (100) interface has the highest energy. This is in qualitative agreement with the solid-liquid interfacial energies calculated for *dc* Si using atomistic simulations [24].

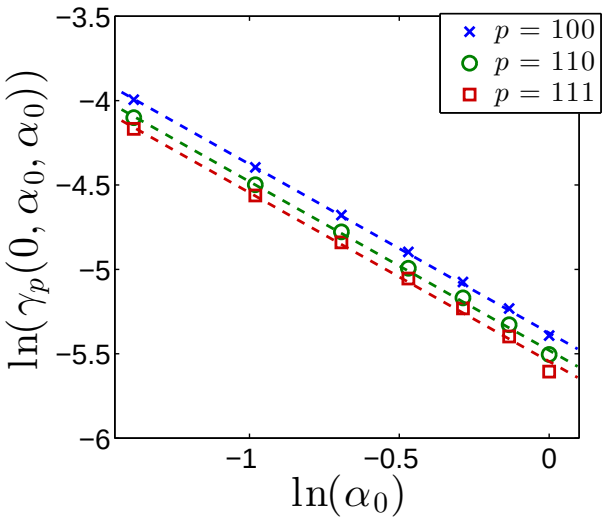

FIG. 5. (Color online) Plots of the natural logarithms of $\gamma_{100}(0,\alpha_0,\alpha_0)$ (blue "×"), $\gamma_{110}(0,\alpha_0,\alpha_0)$ (green circle), and $\gamma_{111}(0,\alpha_0,\alpha_0)$ (red square) for the *dc* free energy used to construct the phase diagram of Fig. 3(d) as a function of the natural logarithms of α_0. Here, $\alpha_1 = \alpha_2 = \alpha_0$ and $\sigma = 0$. The dashed lines are the best fits to the data in the form of Eq. (15).

The dashed lines in Fig. 5 are plots of an inverse power law given by

$$\gamma_p(0, \alpha_0, \alpha_0) = \frac{D_p}{\alpha_0}, \tag{15}$$

where $D_{100} = 4.62 \times 10^{-2}$, $D_{110} = 4.17 \times 10^{-2}$, and $D_{111} = 3.90 \times 10^{-2}$. Figure 5 demonstrates that the simulation results fit well to Eq. (15) with R^2 values of 1.00, 0.999, and 0.999 for D_{100}, D_{110}, and D_{111}, respectively.

C. Solid-Liquid Interfacial Energy Dependence on the Temperature Parameter

In this section, we investigate the dependence of $\gamma_p(\sigma, \alpha_0, \alpha_0)$ on the peak height of the Gaussian functions in the two-body DCF by adjusting σ. Again, we consider the (100), (110), and (111) interfaces. First, we examine the effect of changing σ, while keeping α_0 fixed to 1. The results for these simulations are plotted in Fig. 6. The results show that $\gamma_p(\sigma, 1.0, 1.0)$, decreases with increasing σ.

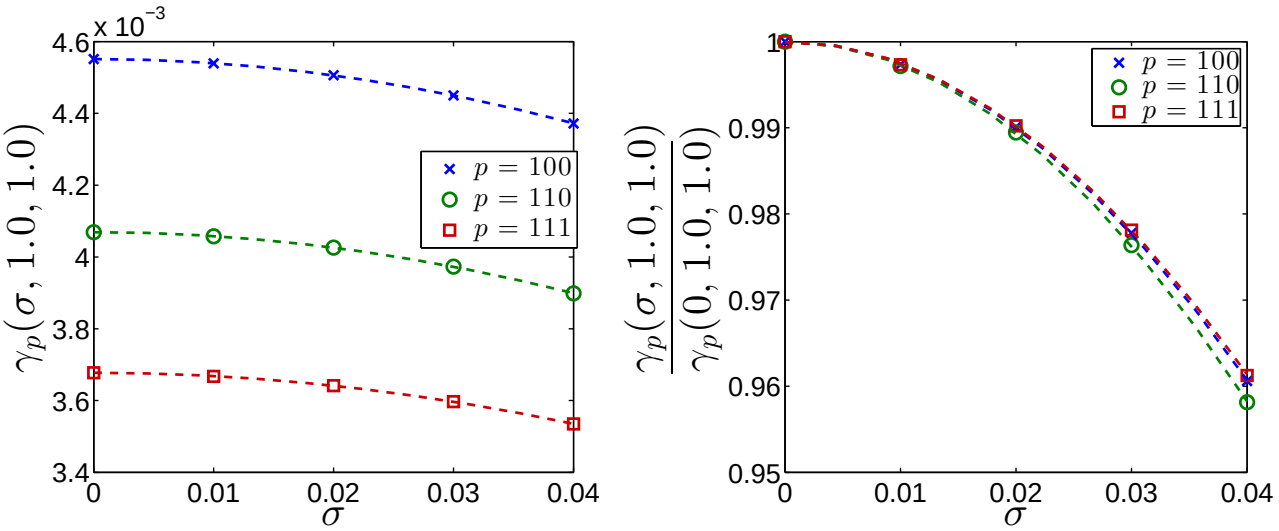

(a) (b)

FIG. 6. (Color online) (a) $\gamma_p(\sigma, 1.0, 1.0)$ and (b) $\gamma_p(\sigma, 1.0, 1.0)/\gamma_p(0, 1.0, 1.0)$ as a function of σ for the (100) (blue "×"), (110) (green circle), and (111) (red square) interfaces. The calculations are for $\alpha_0 = 1.0$ and dashed curves show best fits to the data in the form of Eq. (16).

The dashed curves in Fig. 6 are the best fit curves to the data with a Gaussian function given by

$$\gamma_p(\sigma, \alpha_0, \alpha_0) = \gamma_p(0, \alpha_0, \alpha_0) \exp\left(-b_p(\alpha_0)\sigma^2\right), \tag{16}$$

where $\gamma_p(0, \alpha_0, \alpha_0)$ can be determined from Eq. (15) and $b_p(\alpha_0)$ is a fitting parameter, which depends on the peak width of the Gaussian function, α_0. Note that since the magnitudes of the σ values considered in this analysis are small, a quadratic equation will provide an equally good fit to the data. The plot in Fig. 6(a) shows that the simulation results fit well to Eq. (16), where the fitting constants are determined to be $b_{100}(1.0) = 25.06$, $b_{110}(1.0) = 26.66$, and $b_{111}(1.0) = 24.62$ with R^2 values of 1.00. These values of $b_p(1.0)$ show that the dependence of $\gamma_p(\sigma, 1.0, 1.0)$ on σ is weakest for the (111) interface and strongest for the (110) interface.

In Fig. 6(b), we also plot the scaled values of the interfacial energy, $\gamma_p(\sigma, 1.0, 1.0)/\gamma_p(0, 1.0, 1.0)$, for the same set of data. When scaled in this manner, all interfacial energies have a similar dependence on σ, which is expected from the similar values of $b_p(1.0)$. While the decrease in $\gamma_p(\sigma, 1.0, 1.0)/\gamma_p(0, 1.0, 1.0)$ with respect to σ is greatest for the (110) interface and least for the (111) interface, the differences are very small. This demonstrates that the orientation of the interface normal alters primarily the magnitude of the interfacial energies, but not its dependence on σ.

Next, we examine the dependence of $\gamma_{100}(\sigma, \alpha_0, \alpha_0)$ on σ and α_0. The results for these simulations are plotted in Fig. 7(a). It is evident that the interfacial energies decrease with increasing α_0, which is consistent with our previous results in section IV B. The energies for the (100) interface for $\alpha_0 = 0.25, 0.5$, and 1.0 all decrease with increasing σ, although the changes with respect to σ over the range examined are much smaller than the change due to the different values of α_0.

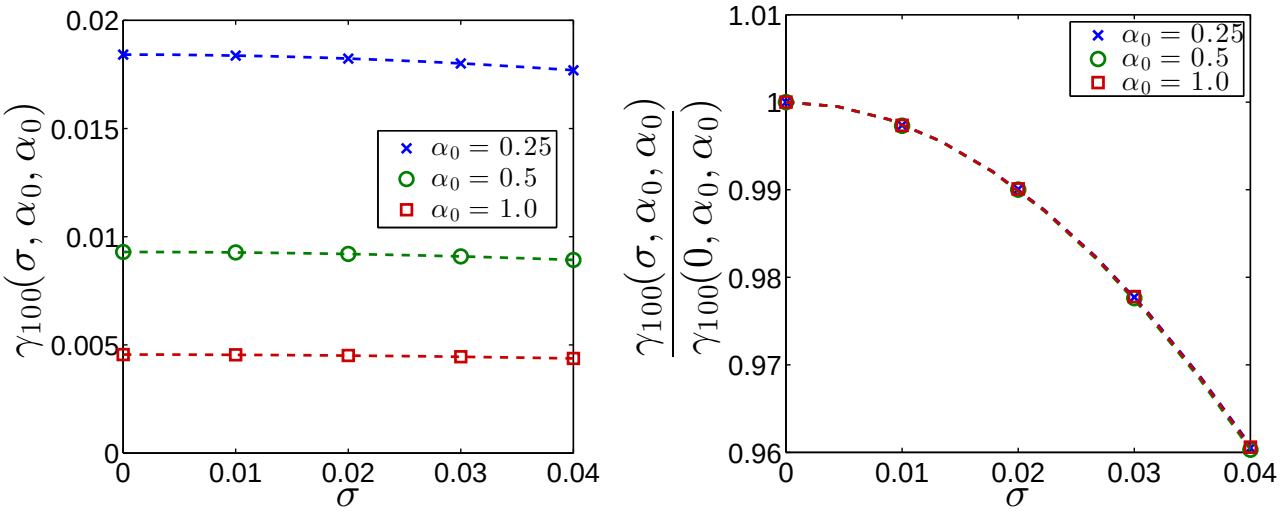

(a) (b)

FIG. 7. (Color online) (a) $\gamma_{100}(\sigma, \alpha_0, \alpha_0)$ and (b) $\gamma_{100}(\sigma, \alpha_0, \alpha_0)/\gamma_{100}(0, \alpha_0, \alpha_0)$ as a function of σ for $\alpha_0 = 0.25$ (blue "$\times$"), $\alpha_0 = 0.5$ (green circle), and $\alpha_0 = 1.0$ (red square). The dashed curves show best fits to the data in the form of Eq. (16).

The dashed curves in Fig. 7 are the best fits to the data with the Gaussian function, Eq. (16). As seen in Fig. 7(a), the simulation results fit well to Eq. (16), with $b_{100}(\alpha_0)$ being approximately 25.13 (specifically 25.13, 25.24, and 25.11 with R^2 values of 1.00 for $\alpha_0 = 0.25$, 0.5, and 1.0, respectively). The decrease in the values of $b_{100}(\alpha_0)$ with increasing α_0 indicates that the dependence of $\gamma_{100}(\sigma, \alpha_0, \alpha_0)$ on σ becomes weaker as α_0 increases.

In Fig. 7(b) we also plot the scaled values of the interfacial energy, $\gamma_{100}(\sigma, \alpha_0, \alpha_0)/\gamma_{100}(0, \alpha_0, \alpha_0)$, for the same set of data. As expected, the values of $\gamma_{100}(\sigma, \alpha_0, \alpha_0)/\gamma_{100}(0, \alpha_0, \alpha_0)$ are essentially identical for all values of α_0; the largest difference between the values of $b_{100}(\alpha_0)$ for $\alpha_0 = 0.25, 0.5$, and 1.0 is less than 1%. Although the analysis in Fig. 7 is for the (100) interface, the negligible dependence of $\gamma_{100}(\sigma, \alpha_0, \alpha_0)/\gamma_{100}(0, \alpha_0, \alpha_0)$ on α_0 is expected to hold for other interface orientations (other values of p) because $\gamma_p(0, \alpha_0, \alpha_0)$ depends on α_0 by the same relationship (Eq. (15)) for all orientations of the interface normal considered.

The negligible dependence of $\gamma_{100}(\sigma, \alpha_0, \alpha_0)/\gamma_{100}(0, \alpha_0, \alpha_0)$ on α_0 suggests that the expression in Eq. (16) can be simplified to

$$\gamma_p(\sigma, \alpha_0, \alpha_0) = \gamma_p(0, \alpha_0, \alpha_0) \exp\left(-\mathcal{R}_p \sigma^2\right), \tag{17}$$

where $\mathcal{R}_p$ is independent of α_0 for each value of p. For the *dc* DCF used in this analysis, $R_{100} = 25.06$, $R_{110} = 26.66$, and $R_{111} = 24.62$. Note that the heights of the Gaussian peaks in the two-body DCF also depend on σ by a Gaussian function, as seen in Eq. (6). The fact that the dependence of $\gamma_p(\sigma, \alpha_0, \alpha_0)$ on σ is also descibed by a Gaussian function suggests that the value of $\gamma_p(\sigma, \alpha_0, \alpha_0)$ is strongly influenced by the height of the peaks in the two-body DCF.

In the analysis of Figs. 6 and 7, the values of $\gamma_p(\sigma, \alpha_0, \alpha_0)$ are calculated within the solid-liquid coexistence region, where $\bar{n}_s$ increases with σ, as seen in Fig. 3. An increase in $\bar{n}_s$ can only arise by adding atoms into the system (by filling vacant sites) because the position of the primary peak of the two-body DCF, k_1, is assumed to be constant, resulting in a fixed lattice spacing for all values of $\bar{n}$ and σ. As a result, $\gamma_p(\sigma, \alpha_0, \alpha_0)$ calculated for each value of σ in Figs. 6 and 7 is for a system containing a different number of atoms. Therefore, the dependence of $\gamma_p(\sigma, \alpha_0, \alpha_0)$ on σ obtained above can be interpreted as that of an open system. We believe the addition of atoms into the system as σ increases is the cause for a decreasing solid-liquid interfacial energy, which is in disagreement with the trend measured experimentally [25, 26] and calculated using atomistic simulations [27–29]

for closed systems. In order to directly compare the dependence of $\gamma_p(\sigma, \alpha_0, \alpha_0)$ on σ from the PFC model to the dependence of $\gamma_p(\sigma, \alpha_0, \alpha_0)$ on melting temperature from experiments and atomistic simulations, it is required to keep the number of particles constant as σ is varied, which is similar to what has been implemented for calculating elastic constants [30]. Therefore, a quantitative comparison between our results and experimental values or those from atomistic calculations cannot be made currently due to the lack of framework for calculations of interfacial energies that are equivalent.

D. Solid-Liquid Interfacial Energy for Unequal Peak Widths

In this section, we investigate how the solid-liquid interfacial energy changes with respect to α_2, when $\alpha_1 \neq \alpha_2$. For our calculations, we set $\alpha_1 = 0.625$ and $\sigma = 0$, while adjusting the values of α_2. These results are plotted in Fig. 8, which shows that $\gamma_p(0, \alpha_1, \alpha_2)$ decreases as the ratio of α_2/α_1 increases for all directions. The dashed lines in Fig. 8 are the best fits for

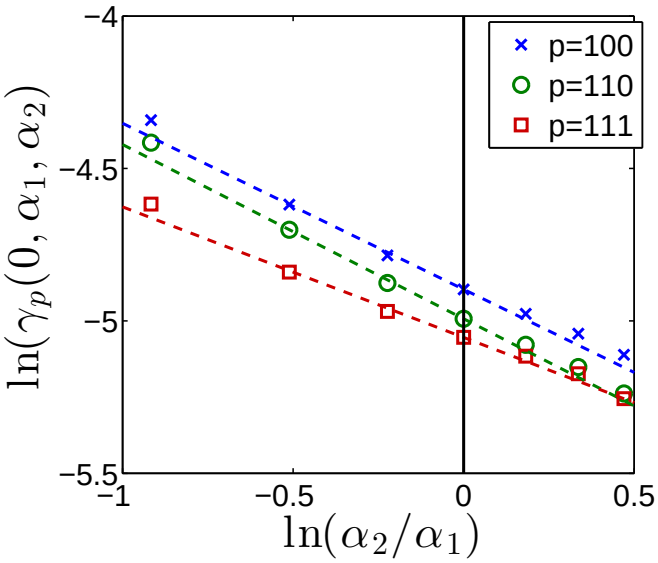

FIG. 8. (Color online) The natural logarithms of $\gamma_{100}(0, \alpha_1, \alpha_2)$ (blue "×"), $\gamma_{110}(0, \alpha_1, \alpha_2)$ (green circle), and $\gamma_{111}(0, \alpha_1, \alpha_2)$ (red square) plotted as a function of the natural logarithms of the ratio α_2/α_1. In these calculations $\alpha_1 = 0.625$ and $\sigma = 0$. The dashed lines show fits to Eq. (18) and the solid vertical line marks the position where $\alpha_2/\alpha_1 = 1$.

the interfacial energies in the form of an inverse power law given by

$$\gamma_p(0, \alpha_1, \alpha_2) = \gamma_p(0, \alpha_0, \alpha_0) \left(\frac{\alpha_2}{\alpha_1} \right)^{-C_p}, \tag{18}$$

where C_p has values of 0.583, 0.611, and 0.463 with R^2 values of 0.982, 0.986, and 0.985 for $p = 100$, 110, and 111, respectively, and $\gamma_p(0, \alpha_0, \alpha_0)$ can be calculated with Eq. (15). Figure 8 demonstrates that Eq. (18) captures the trend of the simulation results; however, the simulation data deviates significantly from the best fit line when α_2/α_1 is far from unity.

These results suggest that Eq. (18) is too simple to fully describe the relationship for the solid-liquid interfacial energy when $\alpha_1 \neq \alpha_2$. Nonetheless, Eq. (18) provides an approximation for $\gamma_p(0, \alpha_1, \alpha_2)$ when $\alpha_1 \neq \alpha_2$ and reduces to Eq. (15) when $\alpha_1 = \alpha_2$. As seen in Fig. 8, $\gamma_p(0, \alpha_1, \alpha_2) < \gamma_p(0, \alpha_0, \alpha_0)$ when $\alpha_2 > \alpha_1$, and $\gamma_p(0, \alpha_1, \alpha_2) > \gamma_p(0, \alpha_0, \alpha_0)$ when $\alpha_2 < \alpha_1$, for all orientations. However, the degree by which $\gamma_p(0, \alpha_1, \alpha_2)$ changes with α_2/α_1 depends on the interfacial orientation. As a result, the relative energies of interfaces will change when the value of α_2/α_1 is far from unity.

V. SUMMARY AND DISCUSSION

We have developed a PFC model with a stable *dc* structure, which is based on the XPFC approach. In this model, we approximate a two-body DCF with a combination of two Gaussian functions in Fourier space, where the first and second peak positions are centered at $k_1 = 2\pi\sqrt{8}/a$ and $k_2 = 2\pi\sqrt{3}/a$, respectively, and a is the lattice constant of a cubic structure. A temperature-density phase diagram, which contains *dc*-liquid, *bcc*-liquid, and *dc*-*bcc* phase coexistence regions, was calculated for the model.

We found that the interfacial energies, $\gamma_p(\sigma, \alpha_1, \alpha_2)$, for the (100), (110), and (111) interfaces depend on α_0 according to an inverse power law when the temperature parameter, σ, is set to zero and the first and second peaks of the DCF are equal, $\alpha_1 = \alpha_2 = \alpha_0$. In the case where $\alpha_1 \neq \alpha_2$, we found that the trend of $\gamma_p(\sigma, \alpha_1, \alpha_2)$ as a function of α_2/α_1 is approximated by an inverse power law. The dependence of $\gamma_p(\sigma, \alpha_1, \alpha_2)$ on σ is well described by a Gaussian function when $\alpha_1 = \alpha_2 = \alpha_0$, via Eq. (17). For all peak widths and interface orientations, the fitting parameter for the Gaussian function, R_p, was found to be within 8% of one another. Therefore, it would be worthwhile to examine whether the dependence of $\gamma_p(\sigma, \alpha_1, \alpha_2)$ on σ for other structures will also exhibit a similar value of R_p.

The relationships developed in our analysis can be used to parameterize the *dc*-PFC model to match interfacial energies to those measured experimentally or calculated with atomistic simulations. However, in order to directly compare the dependence of $\gamma_p(\sigma, \alpha_0, \alpha_0)$ on σ from the PFC model to the dependence of $\gamma_p(\sigma, \alpha_0, \alpha_0)$ on melting temperature from experiments and atomistic simulations, the calculations must be performed for closed systems as σ is varied (i.e., by keeping the number of atoms constant). Such direct comparisons will enable validation of the temperature dependence assumed in the XPFC model.

VI. ACKNOWLEDGEMENTS

This research was supported by National Science Foundation (NSF) under grant No. DMR-1105409. N. Pisutha-Arnond also acknowledges the support of King Mongkut's Institute of Technology Ladkrabang (KMITL) Research Fund under grant number KREF 015803. The calculations in this work was made possible by the computational resources of the Extreme Science and Engineering Discovery Environment (XSEDE), which is supported by NSF grant number ACI-1053575, as well as services provided by Advanced Research Computing at the University of Michigan, Ann Arbor. V. W. L. Chan is grateful for the comments and suggestions of David Montiel and Jason Luce, as well as the discussions with Peter Voorhees, Mark Asta, John Lowengrub, Kevin McReynolds, Timofey Frolov, and Zhen Guan. The authors would also like to thank Elizabeth Hildinger for her help with editing the manuscript.

[1] J. Berry, M. Grant, and K. R. Elder, Physical Review E **73**, 031609 (2006).

[2] J. Berry, K. R. Elder, and M. Grant, Physical Review B **77**, 224114 (2008).

[3] P. Stefanovic, M. Haataja, and N. Provatas, Physical Review E **80**, 046107 (2009).

[4] L. Gránásy, G. Tegze, G. I. Tóth, and T. Pusztai, Philosophical Magazine **91**, 123 (2011).

[5] G. I. Tóth, G. Tegze, T. Pusztai, G. Tóth, and L. Gránásy, Journal of Physics: Condensed Matter **22**, 364101 (2010).

[6] K. R. Elder and M. Grant, Physical Review E **70**, 051605 (2004).

[7] J. Berry, K. R. Elder, and M. Grant, Physical Review E **77**, 061506 (2008).

[8] K. R. Elder, N. Provatas, J. Berry, P. Stefanovic, and M. Grant, Physical Review B **75**, 064107 (2007).

[9] A. Jaatinen, C. V. Achim, K. R. Elder, and T. Ala-Nissila, Physical Review E **80**, 031602 (2009).

[10] N. Pisutha-Arnond, V. W. L. Chan, M. Iyer, V. Gavini, and K. Thornton, Physical Review E **87**, 013313 (2013).

[11] M. Greenwood, N. Provatas, and J. Rottler, Physical Review Letters **105**, 045702 (2010).

[12] M. Greenwood, J. Rottler, and N. Provatas, Physical Review E **83**, 031601 (2011).

[13] M. Greenwood, C. Sinclair, and M. Militzer, Acta Materialia **60**, 5752 (2012).

[14] V. Fallah, J. Stolle, N. Ofori-Opoku, S. Esmaeili, and N. Provatas, Physical Review B **86**, 134112 (2012).

[15] V. Fallah, A. Korinek, N. Ofori-Opoku, N. Provatas, and S. Esmaeili, Acta Materialia **61**, 6372 (2013).

[16] J. Berry, N. Provatas, J. Rottler, and C. W. Sinclair, Physical Review B **86**, 224112 (2012).

[17] M. Lavrskyi, H. Zapolsky, and A. G. Khachaturyan, arXiv.org (2014), 1411.5587.

[18] A. Jaatinen and T. Ala-Nissila, Journal of Physics: Condensed Matter **22**, 205402 (2010).

[19] K. R. Elder, M. Katakowski, M. Haataja, and M. Grant, Physical Review Letters **88**, 245701 (2002).

[20] C. B. Barber, D. P. Dobkin, and H. Huhdanpaa, ACM Transactions on Mathematical Software (TOMS) **22**, 469 (1996).

[21] M. De Graef and M. E. McHenry, *Structural of Materials: An Introduction to Crystallography, Diffraction, and Symmetry* (Cambridge University Press, New York, 2007).

[22] H. Emmerich, H. Löwen, R. Wittkowski, T. Gruhn, G. I. Toth, G. Tegze, and L. Granasy, Advances in Physics **61**, 665 (2012).

[23] J. Towns, T. Cockerill, M. Dahan, I. Foster, K. Gaither, A. Grimshaw, V. Hazlewood, S. Lathrop, D. Lifka, G. D. Peterson, et al., Computing in Science and Engineering **16**, 62 (2014).

[24] P. A. Apte and X. C. Zeng, Applied Physics Letters **92** (2008).

[25] D. Turnbull, Journal of Applied Physics **21**, 1022 (1950).

[26] D. Turnbull, Journal of Chemical Physics **20**, 411 (1952).

[27] B. B. Laird, Journal of Chemical Physics **115**, 2887 (2001).

[28] R. L. Davidchack and B. B. Laird, Journal of Chemical Physics **118**, 7651 (2003).

[29] B. B. Laird, R. L. Davidchack, Y. Yang, and M. Asta, Journal of Chemical Physics **131** (2009).

[30] N. Pisutha-Arnond, V. W. L. Chan, K. R. Elder, and K. Thornton, Physical Review B **87**, 014103 (2013).